University of Crete
Department of Physics

Quantum spin hopping in half-doped manganites

Author:
Andriani Keliri

Supervisor:
Prof. Ilias E. Perakis

Heraklion
February, 2015

Abstract

In the context of a non-equilibrium many-body theory that describes photoinduced femtosecond changes in the magnetic phase of strongly correlated systems, I study two insulating ground states for the case of half-doped manganites: the CE and the FI-CO phase. I numerically derive their energy dispersion for the quantum spin case, for various values of the Jahn-Teller energy and of the spin-canting angle. In addition, I calculate the percentage of spin flips in their valence and conduction band.

Contents

List of Figures

List of Tables

Chapter 1

Introduction

The need for faster devices has drawn attention to manganites, compounds that are strongly correlated electron systems with coupled charge, spin and orbital degrees of freedom. The interplay between strong local interactions produces a rich phase diagram with numerous competing phases (antiferromagnetic insulating, metallic, insulating ferromagnetic or charge ordered antiferromagnetic; to name a few). This makes their physical properties significantly sensitive to external stimuli - such as light or a magnetic field. For instance, these materials change their electrical resistance dramatically in the presence of a magnetic field, so that their magnetoresistance is two or three orders of magnitude larger than that in a typical metal, an effect called colossal magnetoresistance effect (CMR). Moreover, the proximity of insulating and metallic states can make a transition between them occur without the presence of special conditions (of pressure, temperature or composition, as is the case usually).

Recent experiments report the observance of an antiferromagnetic to ferromagnetic ordering in manganites during the application of ultrashort (femtosecond) laser pulses[1]. Using these coherent femtosecond laser pulses to control the magnetic order could help make today's magnetic memory devices a thousand times faster, pushing their switching speed limit from the gigahertz to the terahertz regime.

During the femtosecond pulse, the laser field creates an electron-hole pair on top of the ground state. The dynamics of the system can then either be understood in the basis of classical or quantum spins. Classical spin scenarios neglect spin-flips and suppress electron hopping between antiferromagnetically aligned sites. In the quantum spin case however, photoinduced electron hopping to sites with antiparallel local spin is possible when it is accompanied with spin flips.

In this thesis, I have studied the ground state of these materials in the context of the relevant non-equilibrium many-body theory developed in [1, 2], with my primary goal being to derive their band structure and see how it is dependent on the lattice distortions and spin canting. I considered two insulating ground states: the first is the fairly complex CE phase while the second, the FI-CO phase (charge ordered ferromagnetic insulator), has a simpler orbital ordering.

Chapter 2

Manganites
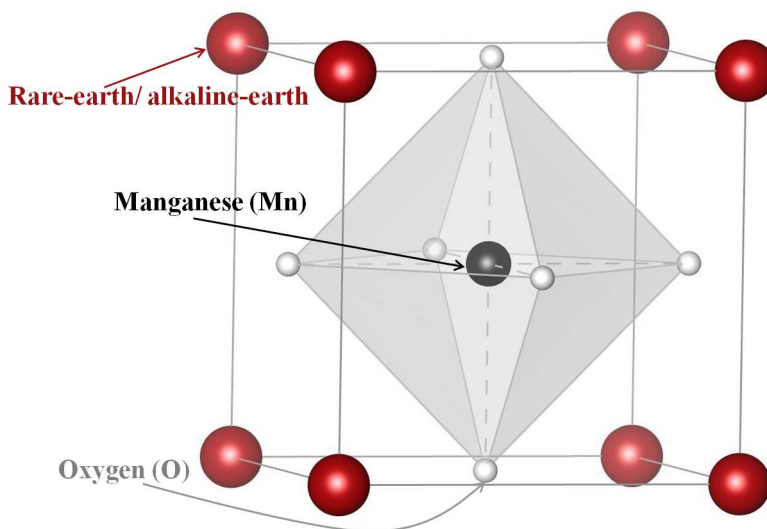
Figure 2.1: The perovskite crystal structure

Interest in manganites first begun in 1950 when G. H. Jonker and J. H. Van Santen published a paper [3] that reported the existence of ferromagnetism in different mixed crystals of manganese oxides.(As Jonker and Van Santen themselves noted, they use the term "manganites" to refer to the mixed valence compounds, although strictly speaking, the term "manganite" applies only to the 100% Mn^{4+} compound.) The general chemical formula of these oxides is $Re_{1-x}A_xMnO_3$, with Re a rare earth ion such as La, Pr, Nd etc., and A an alkaline ion such as Ca, Sr, Ba etc. Oxygen, which is in a O^{2-} state, forms octahedra around the Mn atoms and the relative fraction of Mn^{3+} and Mn^{4+} is regulated by the doping concentration x. The perovskite lattice structure of manganites is illustrated in Figure 2.1.

2.1 Present Interactions

The interaction of the Mn[1] with the surrounding oxygen ions results in the split of its five previously degenerate d-orbitals into two sets (Figure 2.3). The wave functions pointing toward the O^{2-} ions and along the x, y and z axes have a higher overlap with the neighbouring oxygen's p orbitals and thus have a higher electrostatic energy than the d orbitals with a direction between the x, y and z axes [4]. The former, the $d_{x^2-y^2}$ and the $d_{3z^2-r^2}$ orbitals, are called e_g while the latter, the d_{xy}, d_{xz} and d_{yz} are called t_{2g} orbitals (Figure 2.2). Their energy difference, the **crystal field energy** (usually expressed as 10 Dq), has a value of about 1-2 eV [5].
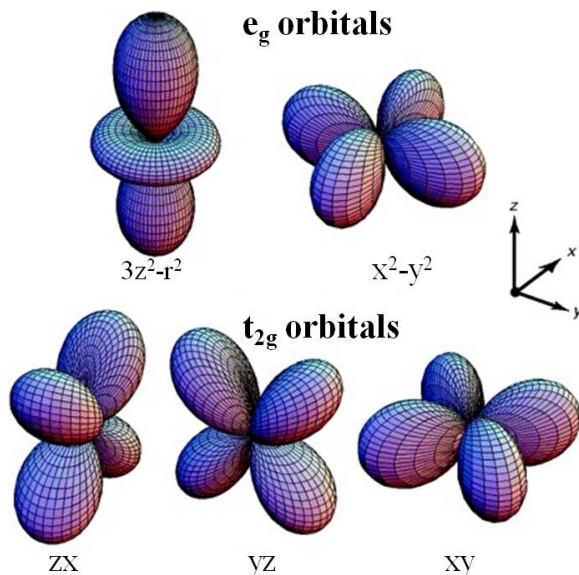
Figure 2.2: The five d orbitals. In the crystal field, their degeneracy is lifted and they are split into two groups; the two e_g and the three t_{2g} orbitals. Figure taken from [4].

The double degeneracy of the e_g orbitals is further lifted due to the distortions of the MnO_6 octahedron, an effect called the **Jahn-Teller effect** (JT) . Which e_g orbital will have the higher energy depends on the distortion (for instance whether the bonds are elongated or shortened along the z-axis). In any case, the higher orbital is labelled a, while the lowest energy orbital is labelled b. A typical value for the Jahn Teller energy (E_{JT}) ranges from 0.5 to 2 eV [6].The distortion is energetically favourable in the Mn^{3+} case because it lowers the occupied e_g level as shown in Figure 2.3. In contrast, Mn^{4+} ions remain undistorted as there aren't any electrons in an e_g orbital to profit from the change in energy. When an e_g electron moves from a Mn^{3+} to a Mn^{4+} ion it carries the JT distortion with it (because in essence, the Mn^{3+} has now become a Mn^{4+} and vice versa), creating a polaron in the process.

---

[1]The electronic structure of Mn is $[Ar]3d^5 4s^2$. Here, Mn will appear only as an ion whose valence is either three (Mn^{4+}) or four (Mn^{3+}).

Figure 2.3: Splitting of the energy levels of the 3d orbitals due to the crystal field and the Jahn-Teller effect.The particular Jahn-Teller distortion (elongation along the z-axis) lifts each degeneracy as shown.

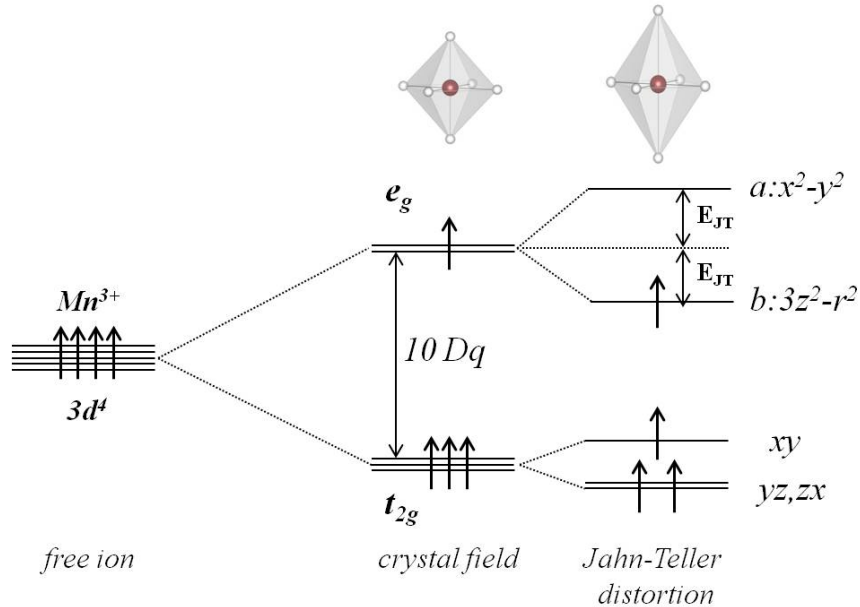Furthermore, there is a strong on site **Coulomb repulsion** amongst e_g electrons, $U \approx$ 5 eV which prevents double occupancy on occupied sites (Mn^{3+}) and the **Hund's rule coupling**, $J_H \approx 1 - 2$ eV between e_g and t_{2g} spins [7] .

The above interactions determine the electron configuration in the ground state of the Mn ions. In the case of Mn^{4+} all of its three d- orbital electrons will populate the t_{2g} orbitals. By application of Hunds rule of maximum multiplicity the spin is maximized in agreement with the Pauli principle, namely all electrons will have parallel spins and will populate a different t_{2g} orbital. The result is a total spin of $S = 3/2$.

Because the crystal field splitting is lower than the energy needed for double occupancy in a t_{2g} orbital (this is known as the weak-field or high-spin case and holds if $10Dq < 5J_H$ [5]), the additional electron in Mn^{3+} occupies an e_g orbital.

2.2   Exchange Mechanisms

The large interatomic distance between the Mn ions (approximately 4 Å) makes direct electronic exchange negligible. Instead, electrons move via the p-orbitals of the oxygen ions. Zener [8] proposed in 1951 a **double exchange** mechanism that allows the movement of charge in manganites and promotes ferromagnetic alignment of neighbouring ions. In a nutshell, double exchange involves a simultaneous hopping of two electrons (hence the name):

an electron moves from an oxygen ion to a Mn^{4+} ion while an e_g electron moves from a Mn^{3+} ion to the oxygen ion (Figure 2.4). Moreover, as shown by Anderson and Hasegawa [9]), the transfer integral for an e_g electron to move from one Mn-site to the next is proportional to $\cos(\theta/2)$, where θ is the angle between the local spins on each site (which are considered classical: as vectors, not as quantum operators). The hopping term is maximized in the case of parallel spins, when $\theta = 0$ and becomes zero when $\theta = \pi$. Because the delocalization of the electrons via hopping decreases the overall energy, the system aligns ferromagnetically to save energy and thus allows the e_g electrons to hop through the crystal.
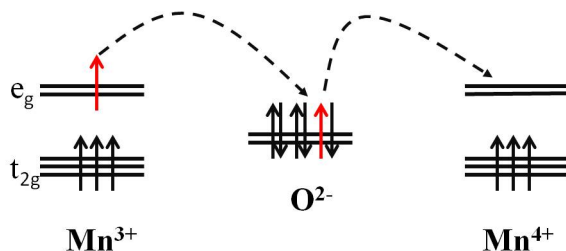
Figure 2.4: Transfer of an electron in the double exchange mechanism from the Mn^{3+} to the Mn^{4+} via the bridging oxygen ion. The transfer favours parallel spin alignment of the Mn t_{2g} local spins.

Apart from the ferromagnetic double exchange there is another indirect exchange interaction at play in manganites, the **superexchange** mechanism. Again, like double exchange, the interaction requires an intermediary (the oxygen ion). However, neighbouring Mn ions can couple via superexchange if they are antiferromagnetically aligned. There is, consequently, a competition between ferromagnetism and antiferromagnetism that arises from the above two mechanisms. Finally, there is also the anisotropic exhange interaction which arises from spin-orbit coupling [10]. When it actes on two spins, it tries to align them at right angles, resulting in **spin canting**, a rotation of the spins by a small angle.

Figure 2.5: The phase diagram of $La_{1-x}Ca_xMnO_3$ shows a plethora of different phases: canted anti-ferromagnetic (CAF), charge ordered anti-ferromagnetic (CO/AFM), ferromagnetic metallic (FM) and ferromagnetic insulating (FI) phase regions. From [5].

Chapter 3

Theory and eigenvalue equation

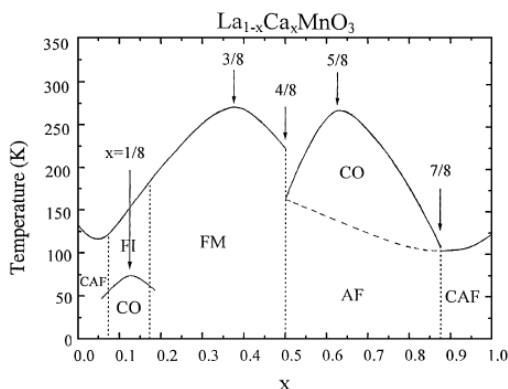In this chapter I follow the theory developed in [1, 2] and will only summarise the relations needed for deriving the results of the following chapters. The theory considers quantum spin fluctuations which allow the e_g electrons to hop to sites with antiparallel t_{2g} spins (in contrast to classical spins that only allow movement between ferromagnetically aligned sites) by simultaneously flipping spin.

The system we are treating is a strongly correlated system where on-site local interactions (U, J_H, JT) are significant (and exceed the kinetic energy). We start from the Hubbard picture: the t_{2g} electrons are considered localized close to individual atoms which are located at sites denoted i in the lattice. Apart from the localized electrons, each site can also be populated by zero (empty site) or one mobile e_g electrons (full site) and is described by eigenstates $|im\rangle$ or $|i\alpha M\rangle$ respectively. M is the z-projection of the total spin J (mobile (e_g) plus local (t_{2g}) spin), whereas $m = -S, ..., S$ is just the z-projection of the local spin S. For our system, the local spin is formed in every site by the three t_{2g} electrons and is always $S = 3/2$ (for the classical spin case, one needs only take the limit $S \to \infty$). The completeness condition for the states requires that at every site

$$\sum_m |im\rangle\langle im| + \sum_{\alpha M} |i\alpha M\rangle\langle i\alpha M| = 1. \tag{3.1}$$

This local constraint excludes multiple occupancy of the e_g levels, namely each site i can either be empty or occupied by one electron - as previously stated. This corresponds to taking the limit $U \to \infty$ (infinite on-site Coulomb repulsion). In addition, the large ferromagnetic Hund's rule coupling J_H between e_g and t_{2g} spins allows only a total spin of $J = S + \frac{1}{2}$ and suppresses states with $J = S - \frac{1}{2}$. We are thus also in the $J_H \to \infty$ limit.

The following density matrices

$$\rho_i(m) = \langle |im\rangle\langle im| \rangle \tag{3.2a}$$

$$\rho_i^\alpha(M) = \langle |i\alpha M\rangle\langle i\alpha M| \rangle \tag{3.2b}$$

give the populations of the empty and the full sites. Each site i is considered to have its own local z-axis (Figure 3.1) that is parallel to the direction of the local t_{2g} spin in equilibrium

(and is either parallel or antiparallel to the laboratory z-axis). The spin canting angles θ_i then describe the tilt of the local axis with respect to the laboratory z-axis. This means that $\theta_i = 0$ implies a spin $\uparrow$ site and $\theta_i = \pi$ for a spin $\downarrow$ site. The e_g electron's spin is then described in reference to the local axis as either $\sigma = 1$ (spin parallel to the local axis), or $\sigma = -1$ (spin antiparallel to the local axis).

Finally, the **eigenvalue equation** is derived:

$$(\omega_{km} - \epsilon_{\beta\sigma}(j))u_{k\sigma}^m(j\beta) = -\sum_{l,\alpha} t_{\alpha\beta}^k(l-j)\sqrt{n_{\beta\sigma}(j)}\sqrt{n_{\alpha\sigma}(l)}\cos\left(\frac{\theta_l - \theta_j}{2}\right)u_{k\sigma}^m(l\alpha)$$

$$+ \sigma\sum_{l,\alpha} t_{\alpha\beta}^k(l-j)\sqrt{n_{\beta\sigma}(j)}\sqrt{n_{\alpha-\sigma}(l)}\sin\left(\frac{\theta_l - \theta_j}{2}\right)u_{k-\sigma}^m(l\alpha) \quad (3.3)$$

The normalizations constants in the eigenvalue equation are defined as:

$$n_{\alpha\uparrow}(i) = \rho_i^\alpha(S + \frac{1}{2}) + \rho_i(S) \tag{3.4a}$$

$$n_{\alpha\downarrow}(i) = \frac{\rho_i(S)}{2S + 1} \tag{3.4b}$$

$n_{\alpha\uparrow}(i) = 1$ since we have excluded double occupancy. $\rho_i(S)$ is non-zero and equal to unity only for empty sites so that $n_{\alpha\downarrow}(i) = 0$ in full sites or $n_{\alpha\downarrow}(i) = \frac{1}{4}$ in empty sites. In the classical spin limit, as $n_{\alpha\downarrow}(i) = 0$ only the first term of equation 3.3 survives and gives the usual hopping amplitudes [5].

The wavevector k is introduced via Bloch's theorem. $t_{\alpha\beta}^k(l-j)$ is the nearest-neighbour hopping amplitude between orbital α of site l and orbital β of site j along the k direction. These hopping amplitudes can be evaluated from the overlap integral between manganese and oxygen ions' orbitals by following [11, 5]. The only integrals that will be needed for calculations here are summarized in table 3.1.
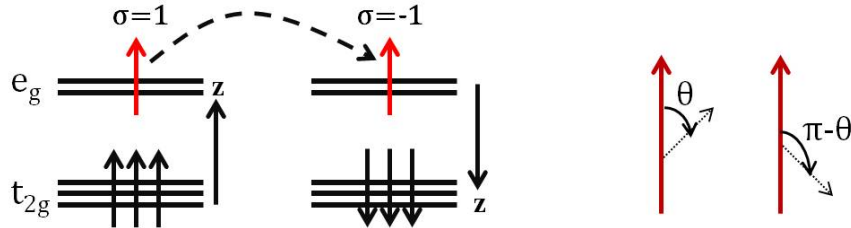

Figure 3.1: The e_g electron's spin is either parallel ($\sigma = 1$) or antiparallel ($\sigma = -1$) to the local axis. Canting can tilt the local axes with respect to the laboratory axis resulting in an angle θ (if the local axis was parallel to the laboratory axis) or $\pi - \theta$ (if it was antiparallel).

Orbitals	Overlap Integral
$x, x^2 - y^2$	$E_{x,x^2-y^2} = \frac{\sqrt{3}}{2} l (l^2 - m^2) V_{pd\sigma}$
$y, x^2 - y^2$	$E_{y,x^2-y^2} = \frac{\sqrt{3}}{2} m (l^2 - m^2) V_{pd\sigma}$
$z, x^2 - y^2$	$E_{z,x^2-y^2} = \frac{\sqrt{3}}{2} n (l^2 - m^2) V_{pd\sigma}$
$x, 3z^2 - r^2$	$E_{x,3z^2-r^2} = l[n^2 - \frac{1}{2}(l^2 + m^2)] V_{pd\sigma}$
$y, 3z^2 - r^2$	$E_{y,3z^2-r^2} = m[n^2 - \frac{1}{2}(l^2 + m^2)] V_{pd\sigma}$
$z, 3z^2 - r^2$	$E_{z,3z^2-r^2} = n[n^2 - \frac{1}{2}(l^2 + m^2)] V_{pd\sigma}$

Table 3.1: Overlap integrals between manganese and oxygen ions. The oxygen p-orbitals (p_x, p_y, p_z) are symbolized by x,y,z; the relevant manganese e_g orbitals by x^2-y^2 and $3z^2-r^2$. $V_{pd\sigma}$ is the overlap integral between the $d\sigma$ and the $p\sigma$ orbital and l,m,n are the direction cosines of the unit vector connecting manganese and oxygen ions. Every other integral needed here can be found by cyclically permuting the coordinates and direction cosines.

To evaluate the hopping amplitude $t^k_{\alpha\beta}(l-j)$ we always need two of these integrals (one for the overlap between the initial orbital β where the mobile electron is situated and an oxygen p-orbital and a second integral for the overlap between the same oxygen p-orbital and the final orbital α). For instance, the hopping amplitude $t^x_{x^2-y^2,x^2-y^2}$ between adjacent manganese ions along the x-axis (via the oxygen's $2p_x$-orbitals) is

$$-t^x_{x^2-y^2,x^2-y^2} = E_{x,x^2-y^2}(1,0,0) \times E_{x,x^2-y^2}(-1,0,0) = \frac{3}{4} t_o, \tag{3.5}$$

where the minus sign is owed to the usual definition of the kinetic energy $(-\sum t^k_{\alpha\beta}(l-j)c^\dagger c)$ and $t_o \equiv (V_{pd\sigma})^2$. Hereafter, I will use t_o as the energy scale; it has a value of about 0.2 to 0.3 eV [6].

Chapter 4

CE phase

4.1 The CE phase

The CE phase at $x = 1/2$ has an equal amount of Mn^{3+} and Mn^{4+} ions and exhibits charge ordering (CO), spin ordering (SO) as well as orbital ordering (OO). Specifically, the manganese ions are arranged as in a checkerboard on the x-y plane (Figure 4.1). Mn^{3+} ions are on the so-called "bridge" sites, whereas Mn^{4+} sites are called "corner" sites. Also, spins align ferromagnetically in zigzag stripes and neighbouring stripes are antiferromagnetically coupled. Finally, following [5], bridge sites have an alternating orbital occupancy of $b = |3x^2 - r^2\rangle \, or \, |3y^2 - r^2\rangle$ and $a = |y^2 - z^2\rangle \, or \, |z^2 - x^2\rangle$, whereas the e_g orbitals on corner sites are the usual $a = |x^2 - y^2\rangle$ and $b = |3z^2 - r^2\rangle$. As previously mentioned, a and b are the antibonding and bonding states. On bridge sites (Jahn-Teller distorted sites), the a and b orbitals are at E_{JT} and $-E_{JT}$ respectively; for corner (undistorted) sites, the a and b orbitals are degenerate at zero energy.
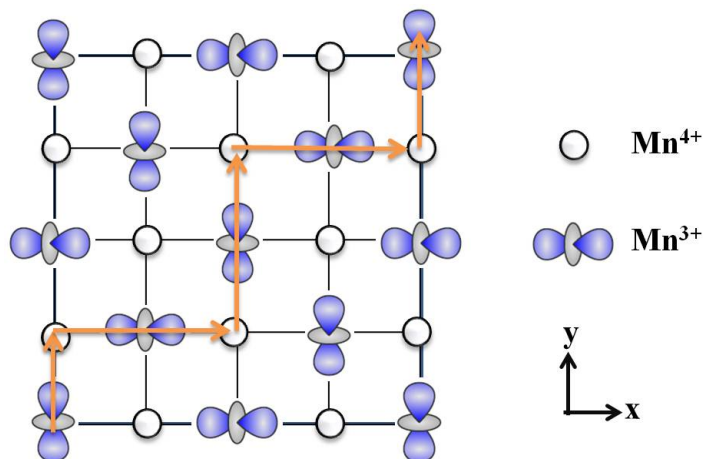

Figure 4.1: The CE phase checkerboard arrangement. Arrows show movement along a zigzag FM stripe.

$$t = \frac{t_o}{4}\left(\begin{array}{c|c} A & B \\ \hline B^* & A \end{array}\right) \tag{4.1a}$$

$$A = \begin{pmatrix}
0 & 0 & 0 & 0 & 3 & -\sqrt{3} & 0 & 0 & 0 & -2\sqrt{3}\Phi_y^* & 0 & 0 & 3\Phi_x & \sqrt{3}\Phi_x & 0 & 2\sqrt{3}\Phi_x\Phi_y^* \\
0 & 0 & 0 & 0 & \sqrt{3} & -1 & 0 & 0 & 0 & 2\Phi_y^* & 0 & 0 & -\sqrt{3}\Phi_x & -\Phi_x & 0 & 2\Phi_x\Phi_y^* \\
0 & 0 & 0 & 0 & 0 & -2\sqrt{3} & 0 & 0 & 3 & -\sqrt{3} & 0 & 0 & 0 & 2\sqrt{3}\Phi_x & 3\Phi_x & \sqrt{3}\Phi_x \\
0 & 0 & 0 & 0 & 0 & 2 & 0 & 0 & \sqrt{3} & -1 & 0 & 0 & 0 & 2\Phi_x & -\sqrt{3}\Phi_x & -\Phi_x \\
3 & \sqrt{3} & 0 & 0 & 0 & 0 & 0 & 0 & 0 & 0 & 3 & \sqrt{3} & 0 & 0 & 0 & 0 \\
-\sqrt{3} & -1 & -2\sqrt{3} & 2 & 0 & 0 & -2\sqrt{3} & 2 & 0 & 0 & -\sqrt{3} & -1 & 0 & 0 & 0 & 0 \\
0 & 0 & 0 & 0 & 0 & -2\sqrt{3} & 0 & 0 & 3\Phi_y^* & -\sqrt{3}\Phi_y^* & 0 & 0 & 0 & 2\sqrt{3} & 3\Phi_y^* & \sqrt{3}\Phi_y^* \\
0 & 0 & 0 & 0 & 0 & 2 & 0 & 0 & \sqrt{3}\Phi_y^* & -\Phi_y^* & 0 & 0 & 0 & 2 & -\sqrt{3}\Phi_y^* & -\Phi_y^* \\
0 & 0 & 3 & \sqrt{3} & 0 & 0 & 3\Phi_y & \sqrt{3}\Phi_y & 0 & 0 & 0 & 0 & 0 & 0 & 0 & 0 \\
-2\sqrt{3}\Phi_y & 2\Phi_y & -\sqrt{3} & -1 & 0 & 0 & -\sqrt{3}\Phi_y & -\Phi_y & 0 & 0 & -2\sqrt{3} & 2 & 0 & 0 & 0 & 0 \\
0 & 0 & 0 & 0 & 3 & -\sqrt{3} & 0 & 0 & 0 & -2\sqrt{3} & 0 & 0 & 3 & \sqrt{3} & 0 & 2\sqrt{3} \\
0 & 0 & 0 & 0 & \sqrt{3} & -1 & 0 & 0 & 0 & 2 & 0 & 0 & -\sqrt{3} & -1 & 0 & 2 \\
3\Phi_x^* & -\sqrt{3}\Phi_x^* & 0 & 0 & 0 & 0 & 0 & 0 & 0 & 0 & 3 & -\sqrt{3} & 0 & 0 & 0 & 0 \\
\sqrt{3}\Phi_x^* & -\Phi_x^* & 2\sqrt{3}\Phi_x^* & 2\Phi_x^* & 0 & 0 & 2\sqrt{3} & 2 & 0 & 0 & \sqrt{3} & -1 & 0 & 0 & 0 & 0 \\
0 & 0 & 3\Phi_x^* & -\sqrt{3}\Phi_x^* & 0 & 0 & 3\Phi_y & -\sqrt{3}\Phi_y & 0 & 0 & 0 & 0 & 0 & 0 & 0 & 0 \\
2\sqrt{3}\Phi_x^*\Phi_y & 2\Phi_x^*\Phi_y & \sqrt{3}\Phi_x^* & -\Phi_x^* & 0 & 0 & \sqrt{3}\Phi_y & -\Phi_y & 0 & 0 & 2\sqrt{3} & 2 & 0 & 0 & 0 & 0
\end{pmatrix} \tag{4.1b}$$

$$B = \begin{pmatrix}
0 & 0 & 0 & 0 & 0 & 0 & 0 & 0 & 0 & 0 & 0 & 0 & 0 & 0 & 0 & 0 \\
0 & -4\theta_z & 0 & 0 & 0 & 0 & 0 & 0 & 0 & 0 & 0 & 0 & 0 & 0 & 0 & 0 \\
0 & 0 & 0 & 0 & 0 & 0 & 0 & 0 & 0 & 0 & 0 & 0 & 0 & 0 & 0 & 0 \\
0 & 0 & 0 & -4\theta_z & 0 & 0 & 0 & 0 & 0 & 0 & 0 & 0 & 0 & 0 & 0 & 0 \\
0 & 0 & 0 & 0 & 0 & 0 & 0 & 0 & 0 & 0 & 0 & 0 & 0 & 0 & 0 & 0 \\
0 & 0 & 0 & 0 & 0 & -\theta_z & 0 & 0 & 0 & 0 & 0 & 0 & 0 & 0 & 0 & 0 \\
0 & 0 & 0 & 0 & 0 & 0 & 0 & 0 & 0 & 0 & 0 & 0 & 0 & 0 & 0 & 0 \\
0 & 0 & 0 & 0 & 0 & 0 & 0 & -4\theta_z & 0 & 0 & 0 & 0 & 0 & 0 & 0 & 0 \\
0 & 0 & 0 & 0 & 0 & 0 & 0 & 0 & 0 & 0 & 0 & 0 & 0 & 0 & 0 & 0 \\
0 & 0 & 0 & 0 & 0 & 0 & 0 & 0 & 0 & -\theta_z & 0 & 0 & 0 & 0 & 0 & 0 \\
0 & 0 & 0 & 0 & 0 & 0 & 0 & 0 & 0 & 0 & 0 & 0 & 0 & 0 & 0 & 0 \\
0 & 0 & 0 & 0 & 0 & 0 & 0 & 0 & 0 & 0 & 0 & -4\theta_z & 0 & 0 & 0 & 0 \\
0 & 0 & 0 & 0 & 0 & 0 & 0 & 0 & 0 & 0 & 0 & 0 & 0 & 0 & 0 & 0 \\
0 & 0 & 0 & 0 & 0 & 0 & 0 & 0 & 0 & 0 & 0 & 0 & 0 & -\theta_z & 0 & 0 \\
0 & 0 & 0 & 0 & 0 & 0 & 0 & 0 & 0 & 0 & 0 & 0 & 0 & 0 & 0 & 0 \\
0 & 0 & 0 & 0 & 0 & 0 & 0 & 0 & 0 & 0 & 0 & 0 & 0 & 0 & 0 & -\theta_z
\end{pmatrix} \tag{4.1c}$$

where $\theta_\alpha = 1 + e^{ik_\alpha a_\alpha}$ and $\Phi_\alpha = e^{ik_\alpha a_\alpha}$ with $(\alpha = x, y, z)$.

4.1.1 The unit cell

The unit cell that is used here involves 16 sites organised in four zigzag chains. It has two planes with identical orbital and charge order but with antiparallel spins. Each plane contains contains two stripes that are antiferromagnetically coupled and each stripe contains four sites: two bridge and two corner sites (Figure 4.2).
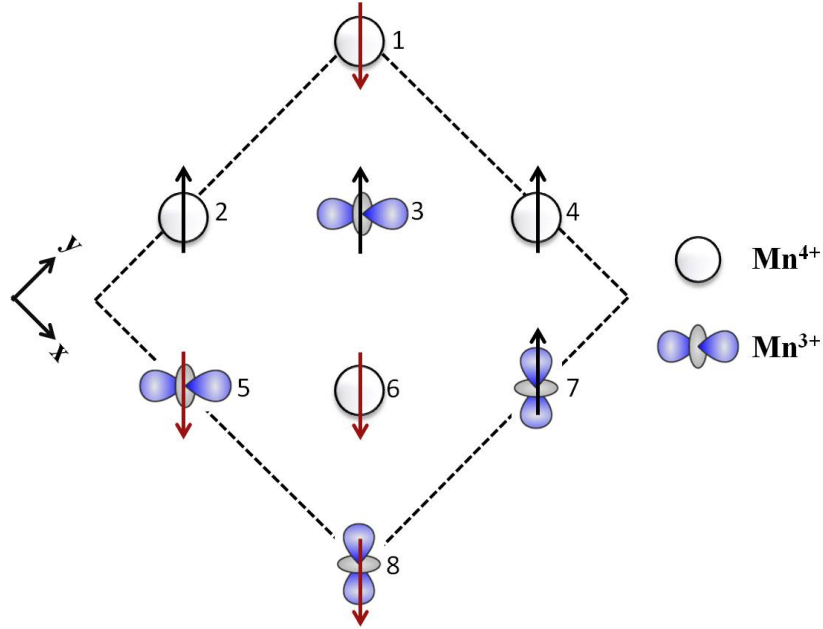

Figure 4.2: The CE phase unit cell contains a total of 16 sites on two planes (8 sites per plane). Here only one plane is shown. The second plane has an identical charge and orbital configuration but antiparallel spins. The red and black arrows show the orientation of the local z-axis.The Bravais lattice parameters are $a_x = a_y = \sqrt{8}a_o$ and $a_z = 2a_o$, where a_o is the distance between two sites. Sites' numbering continues in the same order in the next plane (no. 9 is above no. 1, no. 10 is above no. 2 and so on).

4.2 Numerical results

There are two parameters that define the form of the band structure: the Jahn-Teller energy and the canting angle of the localized t_{2g} electrons' spin. Using the eigenvalue equation (equation 3.3), I construct the Hamiltonian matrix and numerically obtain the corresponding eigenvalues. The hopping elements t_{ab}^k are shown in matrix form in equation 4.1. The Bloch factor $e^{i\vec{k}\cdot\vec{r}}$ is added to the hopping terms to express periodicity. The matrix columns (and rows) are arranged to correspond to the sites in Figure 4.2 in increasing order of their labelled site number. For each site, the first corresponding column is for orbital a and the next for orbital b. Since all calculations for the hopping amplitudes involve either the $|x^2 - y^2\rangle$ or the $|3z^2 - r^2\rangle$ orbital (Table 3.1), it is useful to note the following relations:

$$\left|3x^2 - r^2\right\rangle = -\frac{1}{2}\left|3z^2 - r^2\right\rangle + \frac{\sqrt{3}}{2}\left|x^2 - y^2\right\rangle \tag{4.2a}$$

$$\left|3y^2 - r^2\right\rangle = -\frac{1}{2}\left|3z^2 - r^2\right\rangle - \frac{\sqrt{3}}{2}\left|x^2 - y^2\right\rangle \tag{4.2b}$$

$$\left|y^2 - z^2\right\rangle = -\frac{\sqrt{3}}{2}\left|3z^2 - r^2\right\rangle - \frac{1}{2}\left|x^2 - y^2\right\rangle \tag{4.2c}$$

$$\left|z^2 - x^2\right\rangle = -\frac{\sqrt{3}}{2}\left|3z^2 - r^2\right\rangle + \frac{1}{2}\left|x^2 - y^2\right\rangle. \tag{4.2d}$$

4.2.1   Jahn-Teller energy

For a large Jahn-Teller energy an itinerant electron cannot hop from a Mn^{3+} to a neighbouring Mn^{4+} ion because of their energy level difference (equal to E_{JT}). Consequently, electrons are localized near the atomic levels ($E = \pm E_{JT}$ or $E = 0$) and movement on the xy plane is restricted. This is illustrated in Figure 4.3 where there is little to no dispersion along the x- or y-axis. On the contrary, there is no energy level difference when moving between undistorted (corner) sites along the z-axis. Quantum spins allow this inter plane hopping when it is accompanied by a spin flip (meaning that the photoelectron's spin σ in equation 3.3 changes sign). The result is a large dispersion in the z-direction near the $E = 0$. The large band gap in all directions, close to E_{JT}, indicates an insulating behaviour.
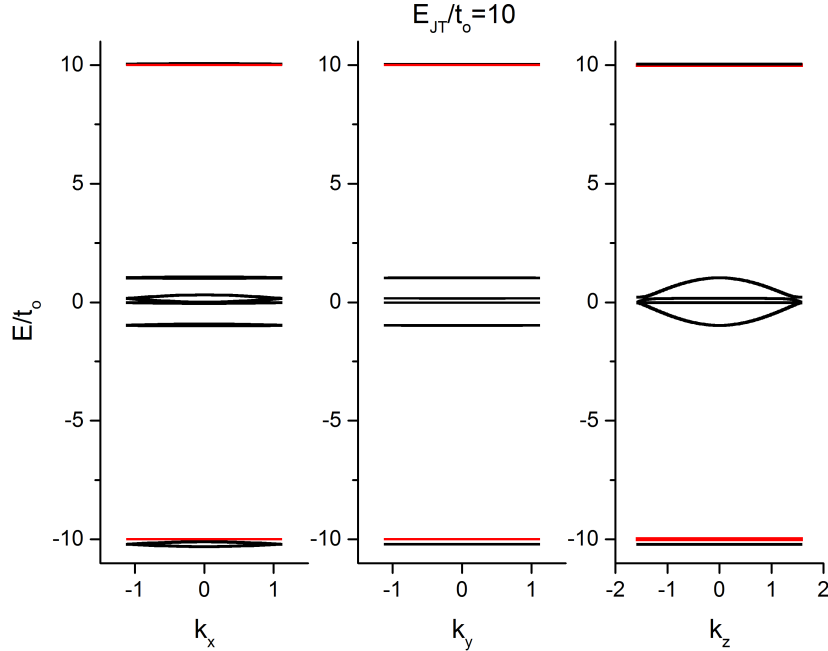

Figure 4.3: Eigenvalues for $E_{JT} = 10t_o$. Red lines show the Jahn-Teller energy. (The canting angle is considered to be $\theta = 0°$ here and for every other graph, unless otherwise stated).

As E_{JT} becomes smaller, electrons can overcome the JT energy to move in all directions and dispersion increases (Figure 4.4). Simultaneously, the gap between valence and conduction band decreases, so that decreasing the E_{JT} favours an insulator-to-metal transition. A comparison of the band structure plotted along high symmetry points, for a large and a small E_{JT} value, is shown in Figure 4.5.
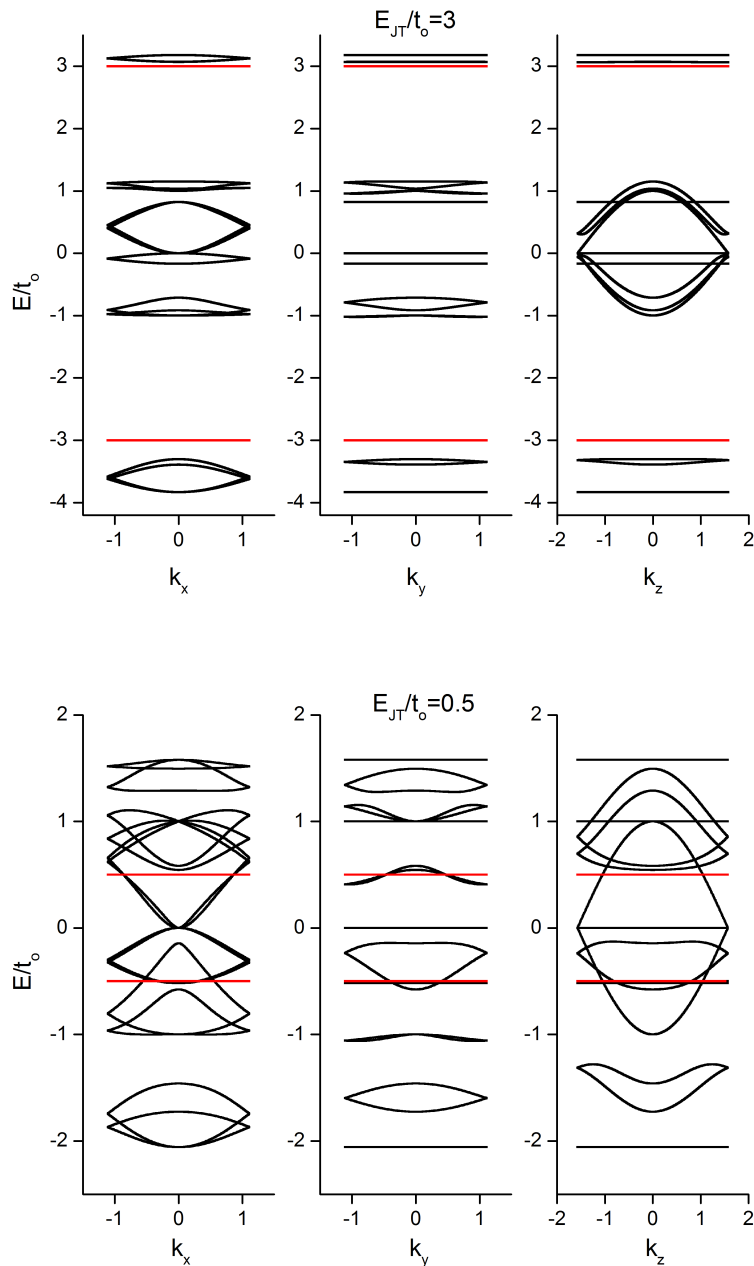

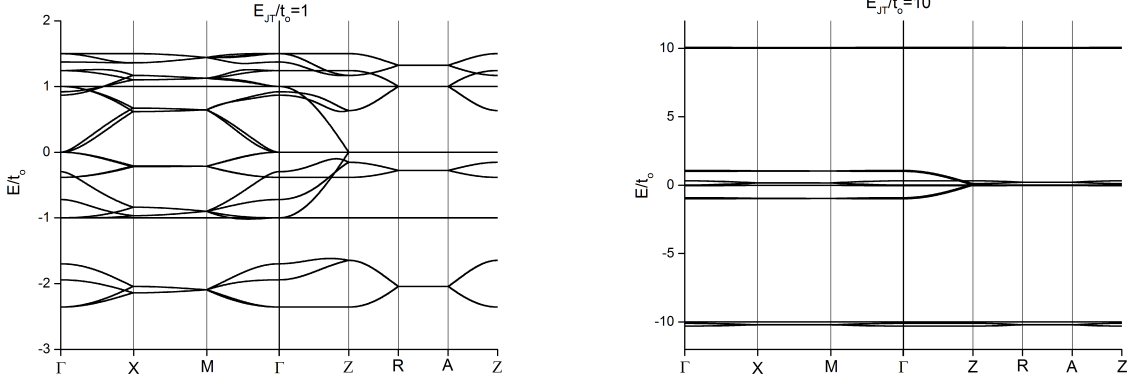Figure 4.4: Eigenvalues for $E_{JT} = 3t_o$ and $E_{JT} = \frac{t_o}{2}$.

Figure 4.5: Band structure for $E_{JT} = t_o$ and $E_{JT} = 10t_o$ plotted along high symmetry points. The high symmetry points are $\Gamma(0,0,0)$, $X(\frac{\pi}{2\sqrt{2}}, 0, 0)$, $M(\frac{\pi}{2\sqrt{2}}, \frac{\pi}{2\sqrt{2}}, 0)$, $Z(0, 0, \frac{\pi}{2})$, $R(\frac{\pi}{2\sqrt{2}}, 0, \frac{\pi}{2})$ and $A(\frac{\pi}{2\sqrt{2}}, \frac{\pi}{2\sqrt{2}}, \frac{\pi}{2})$.

In the classical spin case (e.g. taking the limit $S \to \infty$) there is no coupling between different chains and the e_g electron can only move along a single FM chain. The problem is reduced to a one-dimensional model and thus only the k_x direction shows any dispersion (Figure 4.6). This agrees with previous results[5, 12].
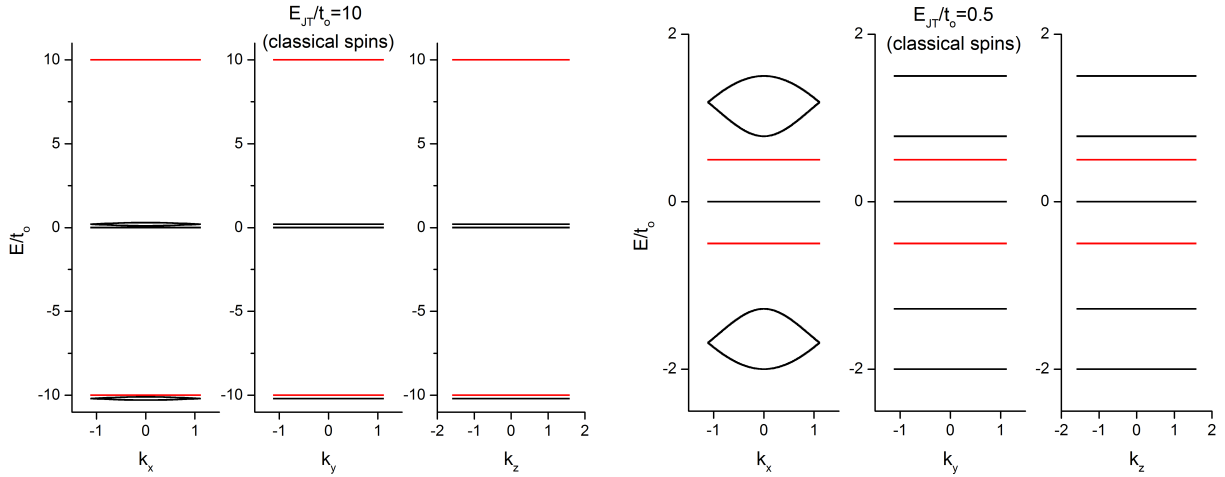

Figure 4.6: Eigenvalues for $E_{JT} = 10t_o$ and $E_{JT} = \frac{t_o}{2}$ in the classical spin case.
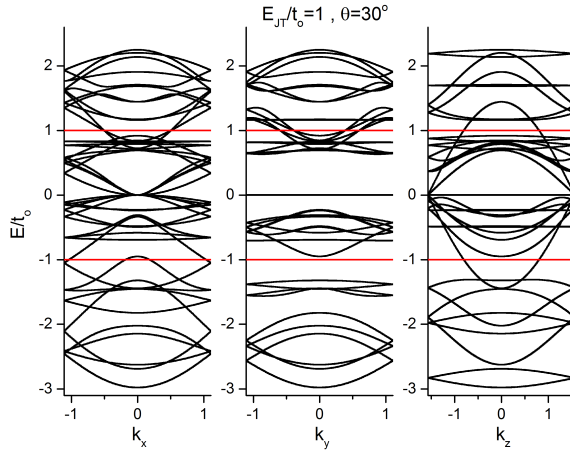
4.2.2 Canting angles

The canting angle essentially models the behaviour of the system when an external magnetic field is present. A large canting angle promotes electron mobility. Specifically, a canting angle $\theta = 90°$ would correspond to ferromagnetic alignment of all core spins and would thus

facilitate movement via double exchange. The result of canting is an increased dispersion (Figure 4.7). At the same time, the conduction-valence gap's value decreases or ,for a sufficiently large angle, closes entirely (as is shown in Figure 4.7b). However, in the system's ground state,the canting angle is small, and to achieve spin-canting of few tens of degrees experimentally, a very large external magnetic field (larger than magnetic fields used in CMR experiments) is required.
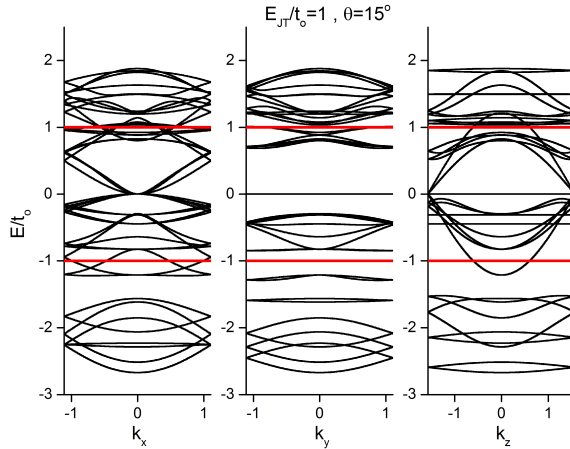
(a) Eigenvalues for $E_{JT} = t_o$ and canting angle $\theta = 15°$.

(b) Eigenvalues for $E_{JT} = t_o$ and canting angle $\theta = 30°$.

Figure 4.7: A larger canting angle lifts degeneracies and facilitates electron movement. Consequently, dispersion increases and the conduction-valence gap's value decreases or vanishes for sufficiently large angles $\theta = 20° - 30°$.

In the classical spin case, in order to get a dispersion similar to the quantum spins' result (where $\theta = 0°$), one needs a large canting angle. For instance, for $E_{JT} = 10t_o$, classical spins

need a $\theta = 30°$ to show the same dispersion in the k_z direction (Figure 4.8). This agrees with previous calculations showing that classical spins require an external magnetic field too large compared to experiments in order to show a phase transition [13].
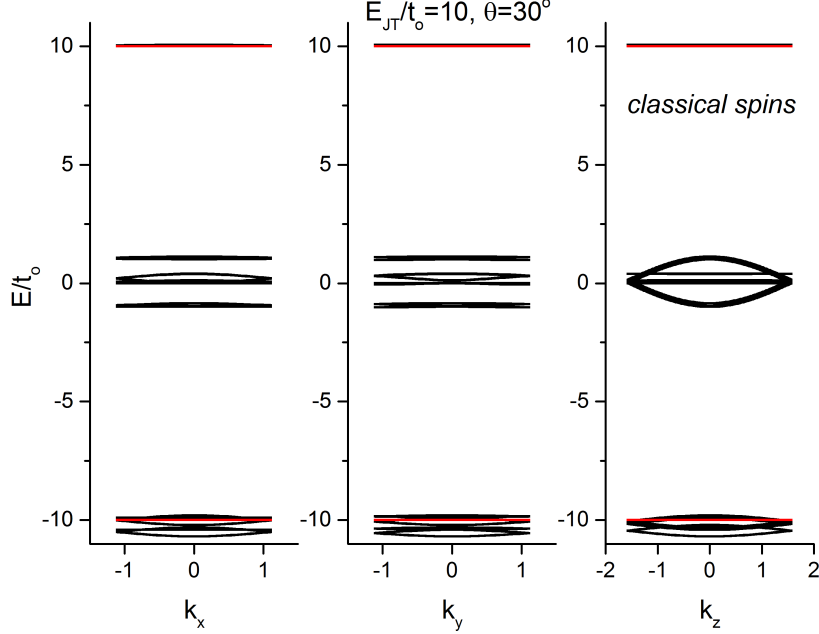

Figure 4.8: Eigenvalues for $E_{JT} = 10t_o$ and classical spins. For $\theta = 30°$ we get a dispersion similar to Figure 4.3.

4.2.3 Eigenstates

The following calculation is a qualitative way to see the contribution of the $\sigma =\uparrow$ and the $\sigma =\downarrow$ populations. A large $\downarrow$ percentage would indicate that photoelectrons move by simultaneously flipping spins. Using equation 3.3, I found the eigenvectors $u_{i\sigma}$ corresponding to an eigenvalue of interest (I focused on the lowest eigenvalue in the valence band and the first eigenvalue in the conduction band) for all sites i, at the $(k_x, k_y, k_z) = (0, 0, 0)$ point and for $\sigma =\uparrow$ (hopping electron spin parallel to the local z-axis) or $\sigma =\downarrow$ (hopping electron spin antiparallel to the local z-axis). Then, I compare the sums $\sum_{i=1}^{16} |u_{i\uparrow}|^2$ and $\sum_{i=1}^{16} |u_{i\downarrow}|^2$ as a function of the Jahn-Teller energy (Figure 4.9) and as a function of the canting angle (Figure 4.10).

In all cases, the valence band shows almost zero percentage of spin flips (Figure 4.9b and 4.10b). In the conduction band however, the picture is vastly different: for $\theta = 0$ and large values of E_{JT}, the $\uparrow$ and $\downarrow$ populations are equal (Figure 4.9a). As E_{JT} decreases, the percentage of spin flips increases until it reaches a maximum at about $E_{JT} = 1.5t_o$. Spin canting facilitates movement without spin flips, so that the $\sigma =\uparrow$ percentage increases with increasing θ (Figure 4.10a).

16
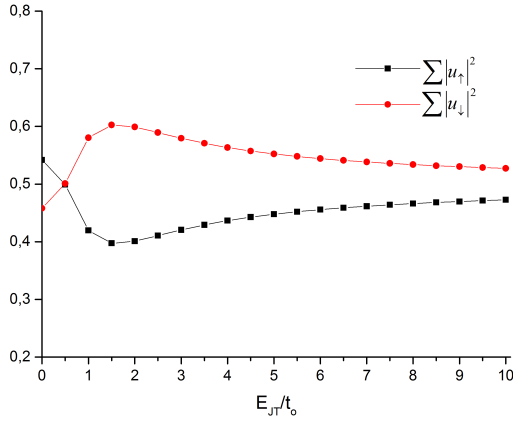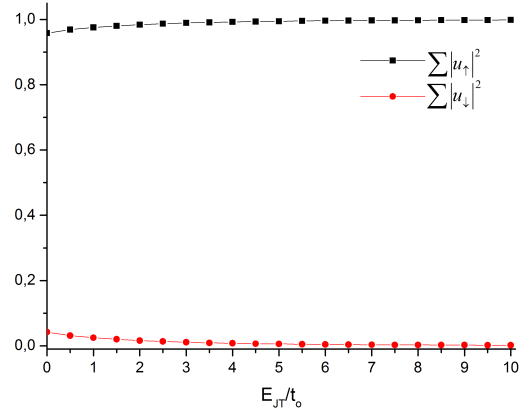
(a) Conduction band

(b) Valence band

Figure 4.9: Contribution of the $\sigma = \uparrow$ and the $\sigma = \downarrow$ populations for various eigenvalues as a function of E_{JT}.
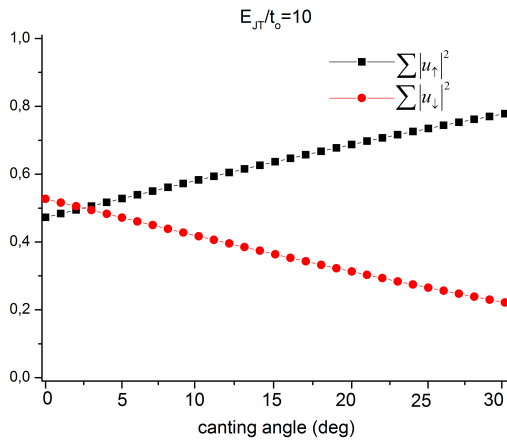

(a) Conduction band
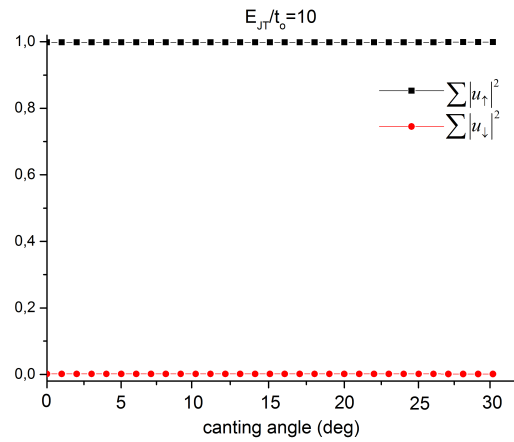
(b) Valence band

Figure 4.10: Contribution of the $\sigma = \uparrow$ and the $\sigma = \downarrow$ populations for various eigenvalues as a function of the canting angle.

17

Chapter 5

FI-CO phase

5.1 The FI-CO phase

The premise of the following calculations is to see if a unit cell without the complicating orbital ordering of the CE phase can show a similar qualitative behaviour. For this, I will consider the FI-CO (charge-ordered ferromagnetic insulating) phase as described in [14].

5.1.1 The unit cell

The FI-CO unit cell (Figure 5.1) is significantly simpler than the unit cell used in the previous chapter. It involves two parallel planes, each consisting of 4 sites. Again, the planes have an antiparallel spin alignment but the same checkerboard charge ordering. Intra plane spins couple ferromagnetically. Following [14], there is also orbital ordering; the JT distorted sites promote the occupancy only of the $|x^2 - y^2\rangle$ orbital at $-E_{JT}$, while in the undistorted sites the doubly degenerate e_g orbitals are the $|x^2 - y^2\rangle$ and $|3z^2 - r^2\rangle$.
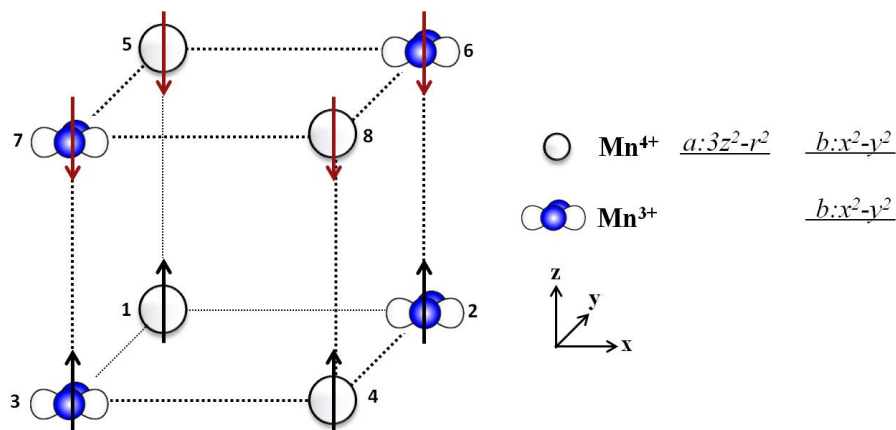

Figure 5.1: The FI-CO phase unit cell contains a total of 8 sites on two planes (4 sites per plane). The Bravais lattice parameters are $a_x = a_y = a_z = 2a_o$, where a_o is the distance between two sites. The red and black arrows show the orientation of the local z-axis.

5.2 Numerical Results

The following calculations repeat the pattern of the previous chapter: I construct the Hamiltonian matrix from equation 3.3 and numerically obtain its eigenvalues. The hopping elements $t_{\alpha\beta}^k$ are shown in matrix form in equation 5.1. Again, the matrix columns (and rows) are arranged to correspond to the sites in Figure 5.1 in increasing order of their labelled site number. When a site is undistorted and has two orbitals (sites 1,4,5 and 8 in Figure 5.1), the first corresponding column is for orbital $a = |3z^2 - r^2\rangle$ and the next for orbital $b = |x^2 - y^2\rangle$.

$$t = \frac{t_o}{4} \left(\begin{array}{c|c} A & B \\ \hline B^* & A \end{array} \right) \tag{5.1a}$$

$$A = \begin{pmatrix} 0 & 0 & \sqrt{3}\theta_x^* & -\sqrt{3}\theta_y & 0 & 0 \\ 0 & 0 & -3\theta_x^* & 3\theta_y & 0 & 0 \\ \sqrt{3}\theta_x & -3\theta_x & 0 & 0 & -\sqrt{3}\theta_y & 3\theta_y \\ -\sqrt{3}\theta_y^* & 3\theta_y^* & 0 & 0 & \sqrt{3}\theta_x^* & -3\theta_x^* \\ 0 & 0 & -\sqrt{3}\theta_y^* & \sqrt{3}\theta_x & 0 & 0 \\ 0 & 0 & 3\theta_y^* & -3\theta_x & 0 & 0 \end{pmatrix} \tag{5.1b}$$

$$B = \begin{pmatrix} -4\theta_z & 0 & 0 & 0 & 0 & 0 \\ 0 & 0 & 0 & 0 & 0 & 0 \\ 0 & 0 & 0 & 0 & 0 & 0 \\ 0 & 0 & 0 & 0 & 0 & 0 \\ 0 & 0 & 0 & 0 & -4\theta_z & 0 \\ 0 & 0 & 0 & 0 & 0 & 0 \end{pmatrix} \tag{5.1c}$$

where $\theta_\alpha = 1 + e^{ik_\alpha a_\alpha}$, $(\alpha = x, y, z)$.

5.2.1 Jahn-Teller energy

Large values of E_{JT} give an image very similar to the corresponding one for the CE phase (Figure 5.2 compared to Figure 4.3). This is expected for a large E_{JT}, because for both the CE and the FI-CO phase hopping is restricted when moving between distorted and undistorted sites but is permitted along the k_z direction from one undistorted site to another.

Smaller values of E_{JT} produce a large dispersion in the k_x and k_y directions (Figure 5.3). Since sites are ferromagnetically aligned in the same plane, the photoelectron moves more easily than in the equivalent case for the CE phase (Figure 4.4), leading to a comparatively larger dispersion. This ferromagnetic intra plane spin coupling of the FI-CO phase also makes the k_x and k_y directions identical.
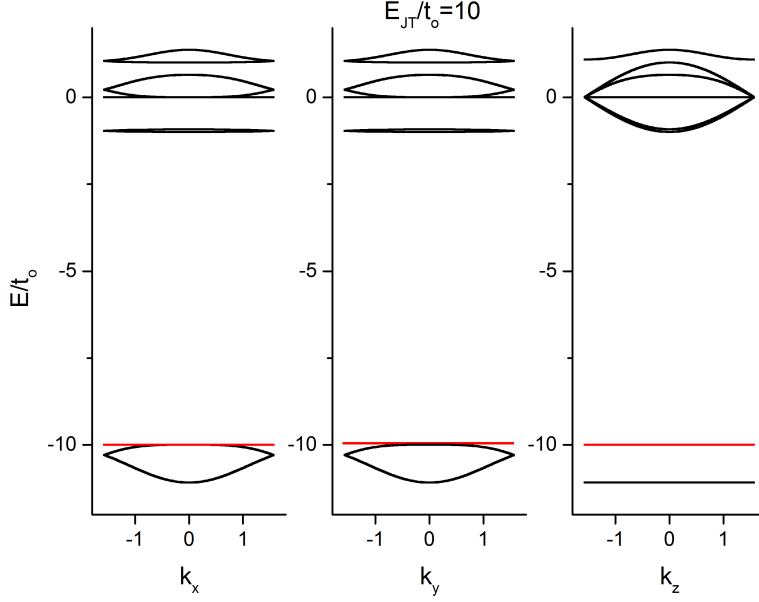
Figure 5.2: Eigenvalues for $E_{JT} = 10t_o$. Large values of E_{JT} produce a very similar band structure with the corresponding ones in the CE phase as the dominating feature of both phases for large E_{JT} is the hopping between $|3z^2 - r^2\rangle$ orbitals along the z-axis, accompanied by a spin-flip.
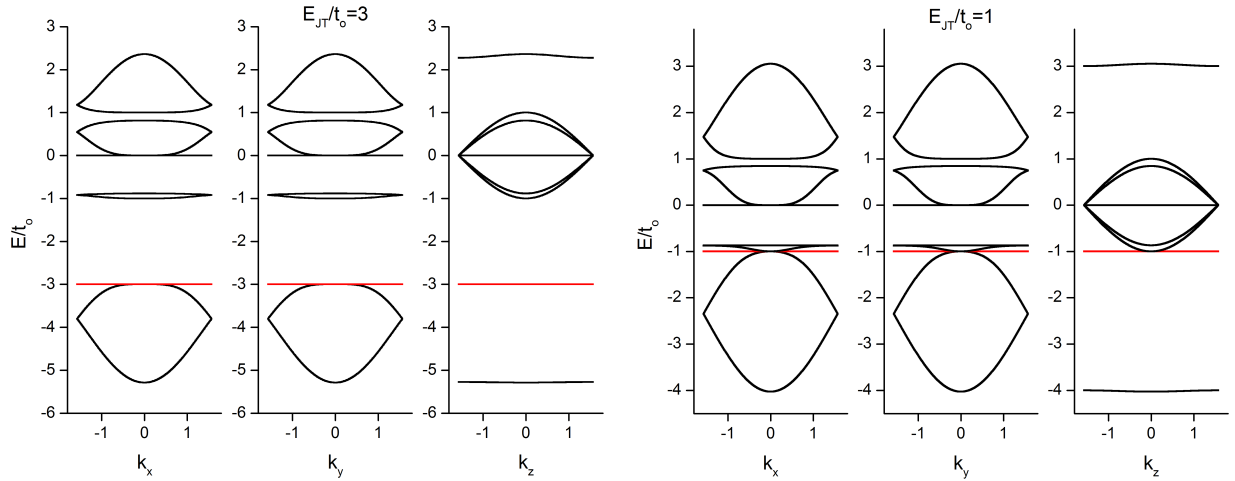

Figure 5.3: Eigenvalues for (a) $E_{JT} = 3t_o$ and (b) $E_{JT} = t_o$. The intra plane ferromagnetic alignment produces a large dispersion in the k_x and k_y directions.

5.2.2 Canting and classical spin limit

Canting in the FI-CO phase doesn't have as much a pronounced effect as it did in the CE phase, except along the k_z direction (Figure 5.4 compared to Figure 4.7). This is to be

expected: an external magnetic field (which tends to align local spins) won't have much to do in the k_x and k_y directions where all t_{2g} spins are already aligned. Along the k_z direction however, canting leads to a significantly increased dispersion.

In the classical spin limit, there is no coupling between different planes (Figure 5.5a) without the presence of magnetic field. Consequently, there is no dispersion in the z direction. In addition,and in agreement with the equivalent conclusion for the CE phase, a large canting angle $\theta \approx 30°$ is needed (Figure 5.5b) in order to achieve a dispersion similar to the quantum spin case (Figure 5.3b).
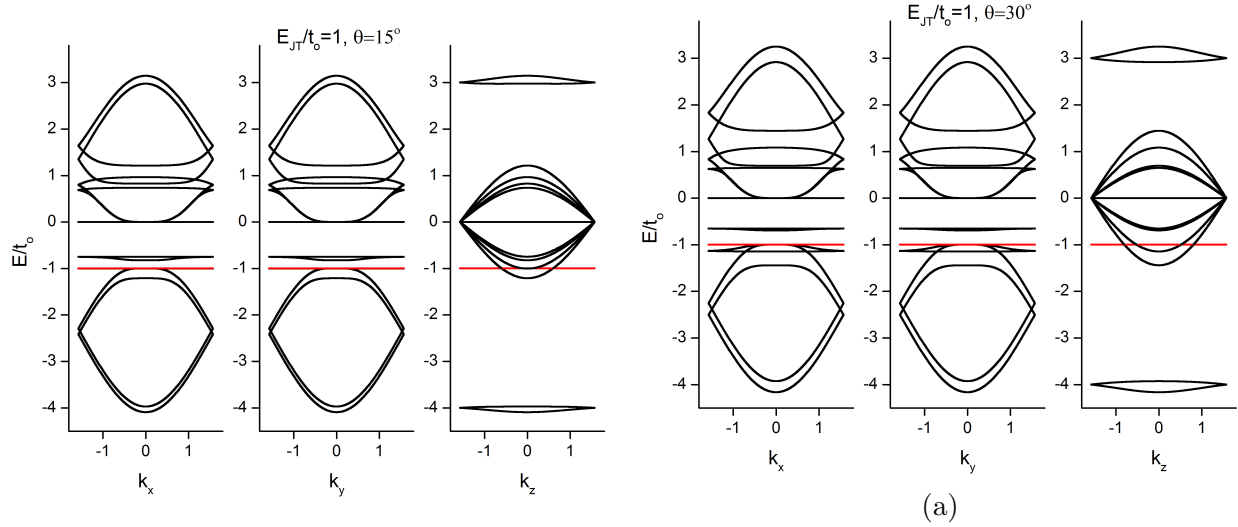

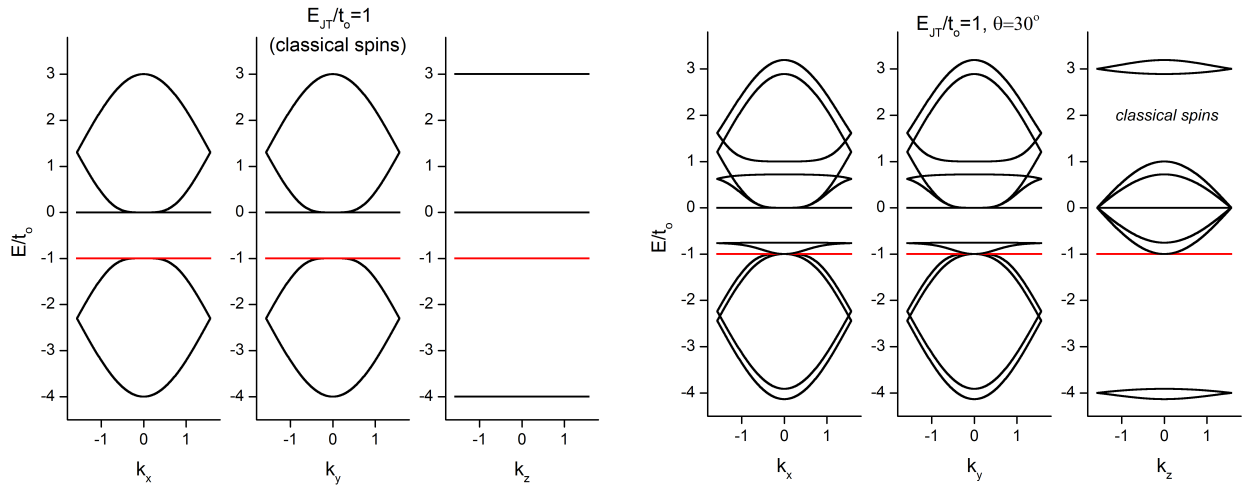Figure 5.4: Eigenvalues for $E_{JT} = t_o$ and canting angle (a) $\theta = 15°$ and (b) $\theta = 30°$.

Figure 5.5: Eigenvalues for $E_{JT} = t_o$ in the classical spin case for canting angle (a) $\theta = 0°$ and (b) $\theta = 30°$.

5.2.3 Eigenstates

The calculations here give almost identical results when compared with the CE phase (Figures 5.6 and 5.7 compared to Figures 4.9 and 4.10 respectively). There is almost zero percentage of spin flips in the valence band (Figures 5.6b and 5.7b), while in the conduction band the ↑ and ↓ populations are equal for $\theta = 0$ (Figure 5.6a). Finally, spin canting increases the $\sigma = \uparrow$ percentage in the conduction band (Figure 5.7a).

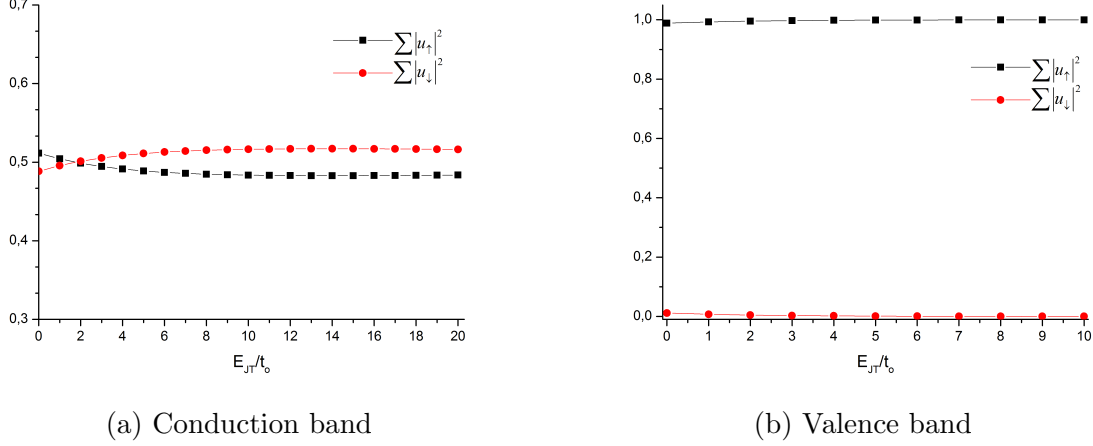(a) Conduction band

(b) Valence band

Figure 5.6: Contribution of the $\sigma = \uparrow$ and the $\sigma = \downarrow$ populations for various eigenvalues as a function of the JT energy.

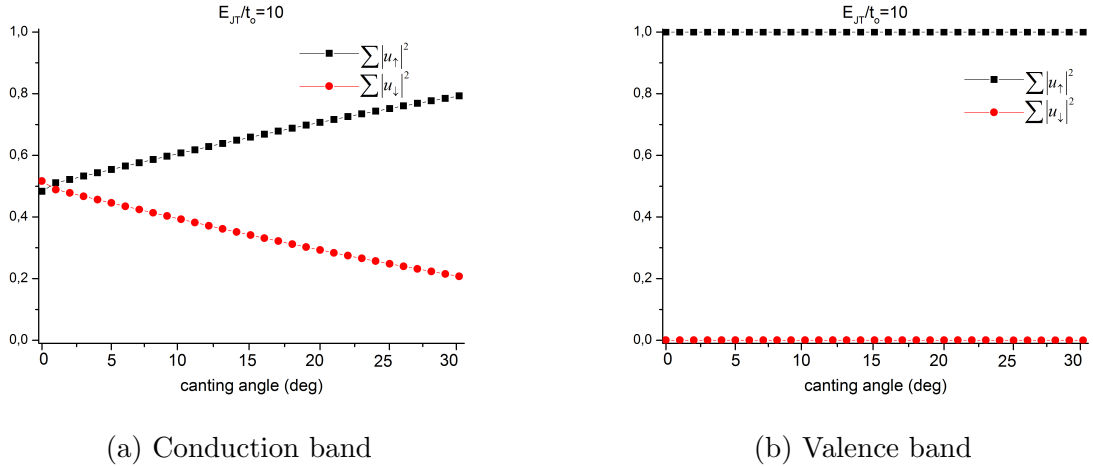(a) Conduction band

(b) Valence band

Figure 5.7: Contribution of the $\sigma = \uparrow$ and the $\sigma = \downarrow$ populations for various eigenvalues as a function of the canting angle.

Chapter 6

Conclusion

In conclusion, I have studied two antiferromagnetic ground states of half-doped manganites, the CE phase and the FI-CO phase, and obtained their band structure for different values of the Jahn-Teller energy (E_{JT}) and the canting angle of the local spins. These two parameters determine the value of the gap between valence and conduction band. Decreasing E_{JT} favours an insulator-to-metal transition, as does a large canting angle.

Unlike classical spin calculations where mobile electrons are confined within one-dimensional ferromagnetic chains, the Hamiltonian used here considers local spins as quantum spins and allows electrons to move between antiferromagnetically aligned sites by simultaneously flipping spins. In the valence band there are almost no spin flips but in the conduction band, the number of spin flips is significant, especially at small values of E_{JT}. Moreover, in contrast with classical spins, quantum spins don't require canting to produce large dispersions. This may explain why classical spin calculations require magnetic fields larger than the ones used in CMR experiments to show a phase transition.

The two phases show a similar qualitative behaviour in response to different values of E_{JT}: a large E_{JT} restricts movement in all directions but quantum spins allow inter plane hopping between Jahn-Teller undistorted sites. This results in a large dispersion in the z-direction around the undistorted sites' energy level ($E = 0$). A smaller value of E_{JT} allows delocalization in all directions and decreases the conduction-valence gap.

Bibliography

[1] T. Li et al., Nature **496**, 69 (2013).

[2] T. Li et al., (2014).

[3] G. Jonker and J. V. Santen, Physica **16**, 337 (1950).

[4] Y. Tokura and N. Nagaosa, Science **288**, 462 (2000).

[5] E. Dagotto, T. Hotta, and A. Moreo, Phys.Rept. **344**, 1 (2001).

[6] T. V. Ramakrishnan, J.Phys.Condens.Matter **19** (2007).

[7] H. Krishnamurthy, Pramana **64**, 1063 (2005).

[8] C. Zener, Phys. Rev. **82**, 403 (1951).

[9] P. Anderson and H. Hasegawa, Phys.Rev. **100**, 675 (1955).

[10] S. Blundell, *Magnetism in condensed matter*, Oxford University Press, 2001.

[11] J. C. Slater and G. F. Koster, Phys. Rev. **94**, 1498 (1954).

[12] S. Dong et al., Phys. Rev. B **73**, 104404 (2006).

[13] O. Cépas, H. R. Krishnamurthy, and T. V. Ramakrishnan, Phys. Rev. Lett. **94**, 247207 (2005).

[14] O. Cépas, H. R. Krishnamurthy, and T. V. Ramakrishnan, Phys. Rev. B **73**, 035218 (2006).